OBSERVATION OF TRAVELLING IONOSPHERIC DISTURBANCES OVER MOROCCO DURING THE GODZILLA SAND AND DUST STORM OF 15TH TO 26TH JUNE 2020 USING GNSS

ABSTRACT

Using Vertical Total Electron Content (VTEC) data from four GNSS receiver stations: IFR1 (Ifrane Seismic), MELI (Melilla), TETN (Tetouan) and OUCA (Ouca) in Morocco, we investigate the Godzilla Sand and dust storm(SDS)event of June 2020as a source of energetics for generation of travelling ionospheric disturbances (TIDs).Godzilla SDS event began on 5th June 2020 in Algeria following a decrease in pressure and spread to other areas across the Saharabetween 6th and 28th June 2020. It was tracked using the Sentinel-5P Satellite mission. Solar wind parameters: Horizontal component of Interplanetary Magnetic Field (IMF Bz), Y-component of Interplanetary electric field (IE-E_y), and solar wind speed (Vz) and geomagnetic indices: Disturbance Storm Time (Dst) and Planetary K (Kp) indices were examined and showed very minimal geomagnetic influence during the period. The study showed that TEC exhibited wave-like structures having distinct troughs and peaks over IFR1-MELI-TETN and OUCA-IFR1-TETN arrays which were clear indicators of generation of TIDs. The arrays and de-trended TEC plots showed that the TIDs propagated poleward. Neutral winds were seen to play a very important role in the propagation of the AGWs which are manifestations of TIDs.

Keywords: Vertical Total Electron Content, Sand and Dust storm, Travelling Ionospheric Disturbances, Atmospheric Gravity Waves

1. INTRODUCTION

Travelling ionospheric Disturbances (TIDs) are known to be signatures of Atmospheric gravity waves (AGWs) in the ionosphere [1, 2]. These wave-like or TID perturbations in the F-layer depends on ionospheric paramaters such as wind, electron density and ion temperature [3].These fluctuations propagate as waves through the ionosphere with wide range of velocities and frequencies. TIDs play an important role in the exchange of energy and momentum between various regions of the upper atmosphere and ionosphere [4].TIDs and AGWsare related in such a way that TIDs are manifestations of AGWs in the atmosphere [3]. This relationship has been highlighted by various notable studies by Hines,[1, 2], Richmond, [5], Hunsucker,[6], Jing & Hunsucker,[7],Hocke & Schlegel,[3].TIDs are triggered bythe ions being forced along the field lines by the neutral air winds driven by the pressure wave[8]. They can also be triggered bygeomagnetic or auroral activity, troposphericactivitiesassociated with earthquakes, tsunami, volcanic eruptions, underground nuclear explosions, seismic events, sand and dust storm (SDS) [4].

Based on their intrinsic properties, TIDs can be categorized either as Large Scale Traveling Ionospheric Disturbances (LSTIDs) or Medium Scale Traveling Ionospheric Disturbances (MSTIDs). LSTIDs have propagation period of 30 minutes to an hour while MSTIDs have propagation period of 15 to 60 minutes. LSTIDs have a wavelength greater than 1000 km and travel with velocities between 300-1000 m/s. MSTIDs have a wavelength of less than 1000 km and travel at a speed of between 100-300 m/s [1, 2, 5, 6, 7].Geomagnetic or aurora activities generate LSTIDs while the lower atmosphere phenomena are a source of MSTIDs [9, 10]. When the AGWs propagate vertically upwards from the lower atmosphere carrying energy, they become unstable and start losing energy. However, their amplitude increases due to reduced air density and mechanical friction [11]. MSTIDs have no correlation with geomagnetic activity. They are known to occur during both daytime and nighttime even though the mechanisms of generations during causing the daytime and nighttime occurrences vary [12].

Daytime MSTIDs are known to originate from lower or middle atmosphere [13]while nighttime MSTIDs originate from electrodynamical processes which include the Perkins instability, that is associated with the E and F region coupling [14]. The climatology of MSTIDs has a strong dependence on longitude[4]. Tsagouri *et al.,* [4]analyzed LSTIDs based on Digisonde observations over European region over Athens (38°N, 23.5°E), Dourbes (50.1°N, 4.6°N) and Ebre (40.8°N, 0.5°E). They observed a significant uplifting of the F2 layer which corresponded with an oscillation pattern in the foF2 during the LSTID activity. Variations in the height of the peak electron density hmF2 and the corresponding scale height Hm were also observed. However, it was difficult to make conclusion on any sensitivity of the method's results to the electric-field-related disturbances which are common in mid-latitudes zone during geomagnetic storms.Habarulema *et al,*[14]investigated the storm time equatorward and poleward LSTIDson global scale. They used total electron content (TEC) observations from GNSS receivers over South American, African and Asian sectors. The results showed the American and African sectors exhibiting predominantly strong poleward TIDs while the Asian sector exhibiting equatorward TIDs which crossed the geomagnetic equator on 9th March 2012.Katamzi & Habarulema, [15]alsoinvestigated TIDs over South African latitudes during the 29th to 31st October 2003 which was a geomagnetically disturbed period, using Global Positioning and System (GPS) observations. The results revealed presence of LSTIDs on the days of the geomagnetic storm using line-of-sightvertical TEC measurements from individual satellites. The wave-like structures were seen to propagate equatorwards with velocities between 587.04 and 1635.09 m/s.

Sand and Dust (SDS) events can be sources of energetics that can lead to generation ofAGWswhich would induce MSTIDs in the ionosphere. The MSTIDs give rise to plasma density gradients as they propagate through the ionosphere leading to electron density instabilities which manifests as TEC variation [16]. An interesting SDS event known as"Godzilla" SDS which occurred between 1st June and 30th June 2020 across the Sahara desert was tracked bythe Copernicus Sentinel-5P satellitewhich stores a variety of satellite images used to detect changes in landscape[17] and the offline Satellite Absorbing Index (SAI), which qualitatively shows elevated aerosol layers in atmosphere [18]. The National Oceanic and Atmospheric Administration (NOAA) approximated the Godzilla SDSto be between 60% to 70% larger than the Sand and dust storms experienced in the past [19]. The greatest impact of the Godzilla SDSwas felt between 15th and 20th June 2020 [20, 21. 22].

In the present paper, we investigate and present results for thepropagation characteristics of AGWs associatedwith the Godzilla SDS event that occurred between 15th and 26th June 2020 over Morocco.The study is investigatedwithin a geomagnetically quiet period, hence geomagnetic storm-related phenomena is eliminated. We analyze GPS-TEC data from four Global Navigation Satellite System (GNSS) receiver stationssituated in Morocco.

2. DATA SOURCES AND METHODOLOGY

2.1 Geomagnetic indices data and solar wind parameters

In this study, the periods between 15th and 26th June 2020 were considered due to greatest intensity of the Godzilla SDS event over Morocco[20]. The geospace conditions such as Kp index showing the level of the geomagnetic activity, the hourly values of Z-component of the interplanetary magnetic field (IMF-Bz), Y-component of the interplanetary electric field (IEFy), solar wind speed (Vz), Planetary K (Kp) and Disturbance storm time (Dst) indices were considered during these periods. However, these parameters were obtained from the archive of OmniWeb website via *https://omniweb.gsfc.nasa.gov/form/dx1.*

2.2 Godzilla SDS data

The movement of the Godzilla SDS over Morocco was tracked using the Copernicus Sentinel-5P satellite mission which was launched by the European Space agency on 13th October 2017. This satellite uses the Google Earth Engine (GEE), which is a cloud-based platform that stores a variety of satellite images used to detect changes in landscape [23]and the Sentinel-5P Aerosol Index (SAI), which qualitatively shows elevated aerosol layers in atmosphere and the Sentinel-5P Aerosol Index (SAI), which qualitatively shows elevated aerosol layers in atmosphere [18].

2.3 IGS data

The GPS-TEC data were obtained fromfour GNSS receiver stations in Morocco as shown in the map displayed in Figure 1 below with the station's geographical locations. Table 1 shows the station codes, the station names, geographical and geomagnetic coordinates, and their respective local time. The GPS-TEC data were accessed from the University of NAVSTAR Consortium dual frequency website: *http://unavco.org/data/gps-gnssdata/*.

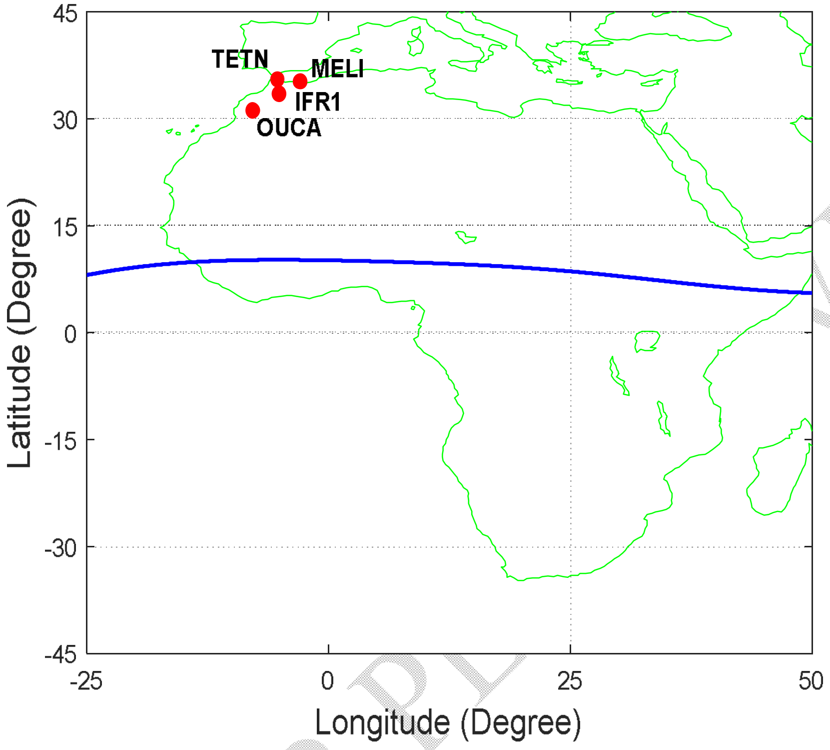

Figure 1: Geographic locations of the the four GNSS receiver stations over Morocco

The GPS-TEC data in the IGS receivers is usually saved in the zipped Receiver Independent Exchange (RINEX) Format which is converted to GPS observable files usingappropriate software [24]. In this study, the Gopi software developed by Prof Gopi Krishna Seemala[25]was used to convert the RINEX to observation files. These GPS measurements are either code pseudoranges (P) or carrier phases (ϕ). The receiver receives the code time delay and carrier phase difference by cross-correlating the f_1 and f_2 modulated carrier signals, which are normally considered to travel along the same path through the ionosphere[26]. Estimates of GPS-derived ionosphericTEC can be obtained using dual frequency GPS measurements [27, 28]. GPS receiver data is critical for estimating the electron density along a ray path between a GPS satellite and a ground receiver [29, 30]. Dual-frequency GPS receivers may offer integral information on the ionosphere and plasmasphere. This is done by computing the differential of the code and carrier phase measurements, in addition to removing ionospheric inaccuracies in TEC estimates[31, 32]. As a result, the GPS-TEC computed by the dual-frequency receivers is offered as an input to an ionosphere assimilation model[33]. For the present study, GPS-TEC data collected in dual-frequency receivers was used. The GPS-TEC data was obtained using the pseudo-range and carrier phase measurements. The TEC calculated from the pseudo-range measurement (slant TEC) is given by Equation 1:

$$STEC = \frac{1}{40.3}\left[\frac{f_1^{\,2} f_2^{\,2}}{f_1^{\,2} - f_2^{\,2}}\right](P_2 - P_1)\ (1)$$

Similarly, the TEC from carrier phase measurement may be calculated as follows using Equation 2:

$$STEC = \frac{1}{40.3}\left[\frac{f_1^{\,2} f_2^{\,2}}{f_1^{\,2} - f_2^{\,2}}\right](\phi_2 - \phi_1)\ (2)$$

where f_1 and f_2 are GPS satellite frequencies determined from the fundamental frequency, f_o= 10.23MHz as: (f_1=154, f_o=1,575.42MHz, (f_2=120, f_o=1,227.60 MHz), and the differential code and phase measurements are (P_2– P_1) and (ϕ_1– ϕ_2), respectively [34]. The vertical total electron content (VTEC) is obtained using the relations in Equation 3:

$$VTEC = STEC \times Cos(\chi')\ (3)$$

where the zenith angle χ' is given by Equation 4:

$$\chi' = \arcsin\left[\frac{R_E \cos\alpha}{R_E + h} Sin(\chi)\right]\ (4)$$

VTEC is therefore given by equation 5:

$$VTEC = STEC\left\{\cos\left[\arcsin\left(\frac{R_E \cos\alpha}{R_E + h}\right)\sin(\chi)\right]\right\}\ (5)$$

Where α is the satellite's elevation angle, $R_E$is the Earth's mean radius, and h is the height of the ionospheric layer, which is considered to be 400 km.

To reduce multipath effects, the data selected was for elevation angles of 30° and above [35].

Information for the four GNSS receiver stations: MELI, IFR1, OUCA and TETN is given in Table 1:

Table 1: information of the geographical and geomagnetic locations of the stations over Morocco

stationcode	StationName	Geographic Latitude	Geographic Longitude	Geomagnetic Latitude	Geomagnetic Longitude	Local Time
MELI	Melilla	35.28°N	2.95°W	25.64°N	77.44°W	UT+1
IFR1	IfraneSeismic	33.52°N	5.13°W	23.14°N	79.03°W	UT+1
OUCA	Ouca	31.206°N	7.87°W	20.04°N	81.12°W	UT+1
TETN	Tetouan	35.56°N	5.36°W	26.15°N	79.51°W	UT+1

The average daily data of VTEC for all PRNs for IFR1, MELI, OUCA and TETN for all the days between 15th and 26th June 2020 were obtained by averaging the VTEC values for all identical pseudo-random numbers (PRNs) within a 24 hour period [36]and used to plot VTEC against Universal Time (UT) for each day and station. The VTEC against UT plots for each day were analyzed.

2.3 Methodology

Extracting travelling Ionospheric disturbances (TIDs)from GPS-TEC data

Background or unperturbed ionospheric TEC was determined by fitting each satellite's time series of the VTEC data with a fourth polynomial across all the four GNSS receiver stations. This was done using equation 1.

$$VTEC_{fit} = at_{ij}^{4} + bt^{3}ij + ct_{ij}^{2} + dt_{ij} + \varepsilon \quad (1)$$

where $VTEC_{fit}$ is fitted VTEC at time *t*,*i*= 1, 2, 3,4. (No of receiver stations), *j*=1, 2, ……, 32 (the number of satellites),Ɛ is the residual error of the fitting process and coefficients *a, b, c* and *d* are obtained using least squares method[14].

High frequency changes in ΔVTEC due to irregular ionospheric plasmawas detected by finding the difference between actual VTEC data and modeled data using equation 2.

$$\Delta VTEC = VTEC - VTEC_{fit} \quad (2)$$

where, ΔVTEC = deviation of VTEC

VTEC = actual VTEC data at time t

$VTEC_{fit}$ = modeled data

ΔVTEC gives information about the spectral content of the signal and how it changes with time. Plots of VTEC verses UT were plotted alongside their corresponding ΔVTEC verses UT plots.The potential wavelike structures were monitored across the across three stations along close latitudes. In this case, two receiver arrays were considered: OUCA-IFR1-TETN and the IFR1- MELI-TETN receiver arrays. The amplitudes of the wavelike structures (TIDs) that modulate TEC were inferred by monitoring ΔVTEC[14, 37].

Detrended TEC from GPS-TEC data was created using the Savitzky-Golay filter with a 60 minute sliding window for all the four GNSS receiver stations and visible satellites [38]. The Savitzky-Golay filter uses quadratic polynomial that is fitted over each sliding window. The detrended TEC over all geographic latitudes against Universal time (UT) were directly constructed in a temporal resolution of 10 minutes. The derived detrended TEC plotsalong geographical latitudes were then used to investigate propagation behavior of the Godzilla SDS induced TIDs[39].

3. RESULTS AND DISCUSSIONS

3.1. The movement of the Godzilla SDS between 15th and 26th June 2020 over Sahara

The movement of the Godzilla SDS over Morocco between 15th and 26th June 2020 was tracked using the Copernicus Sentinel-5P satellite.Between 15th and 26th June 2020, the Western part of Africa such as Mauritania, Mali, Morocco and Western Sahara felt the greatest impact of the Godzilla SDS [2] as in Figure 2 and 3. By 20th June 2020, the first traces of dust had reached the Caribbean [40]. Large SDS traces were observed over the upper parts of the Sahara between 21st June and 26th June 2020as shown in Figure 3.

In Figures 2 and 3, the cream colour on the SAI indicates low aerosol concentrations in the atmosphere while red colour shows presence of high aerosol concentrations in the atmosphere during the Godzilla SDS of June 2020 as tracked by the Copernicus Sentinel-5P satellite.

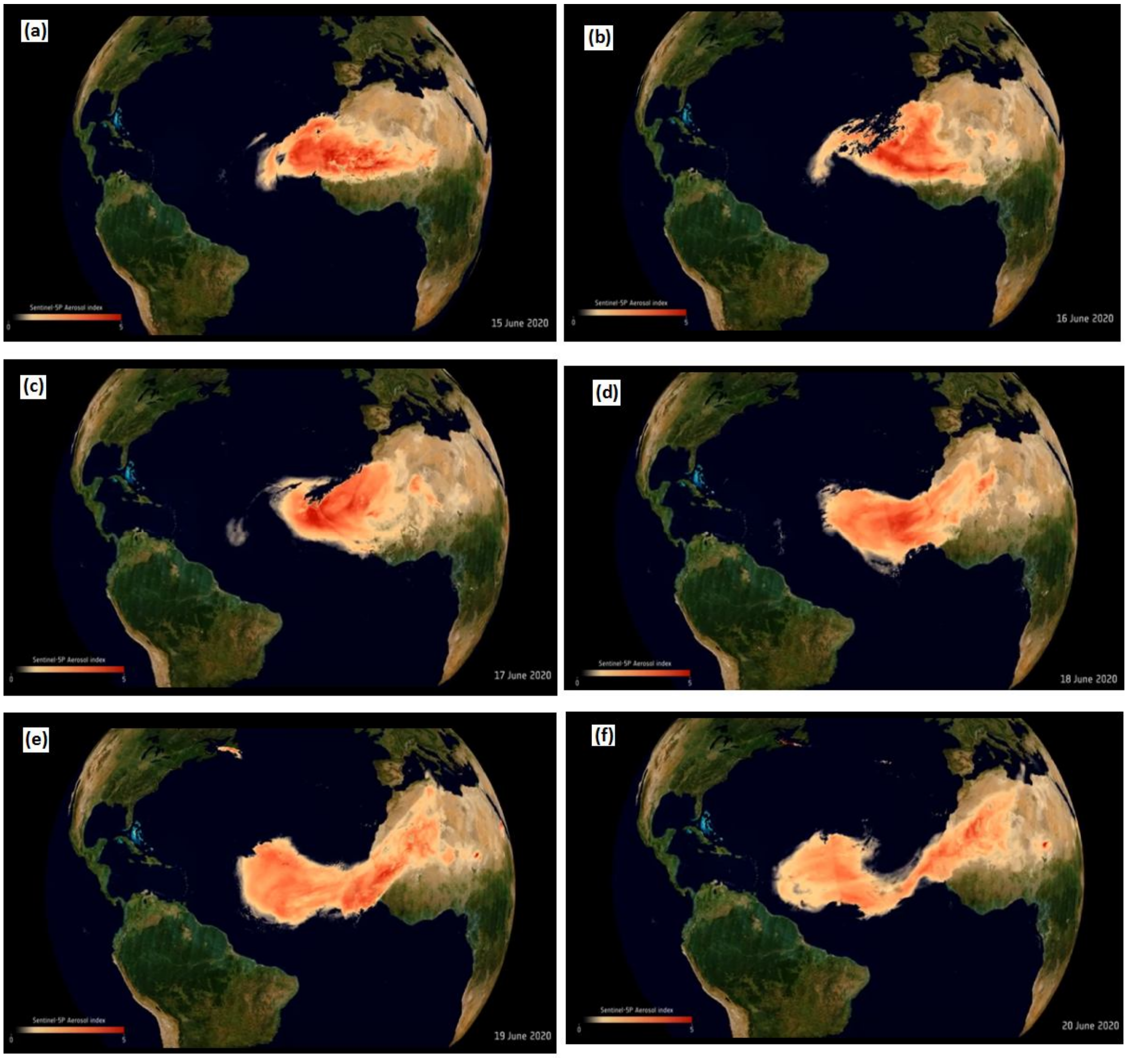

Figure 2: The Copernicus Sentinel-5P satellite images of Godzilla SDS over the Sahara for (a) 15.06.2020 (b) 16.06.2020 (c) 17.06.2020 (d) 18.06.2020 (e) 19.06.2020 (f) 20.06.2020 (European space Agency, 2020)

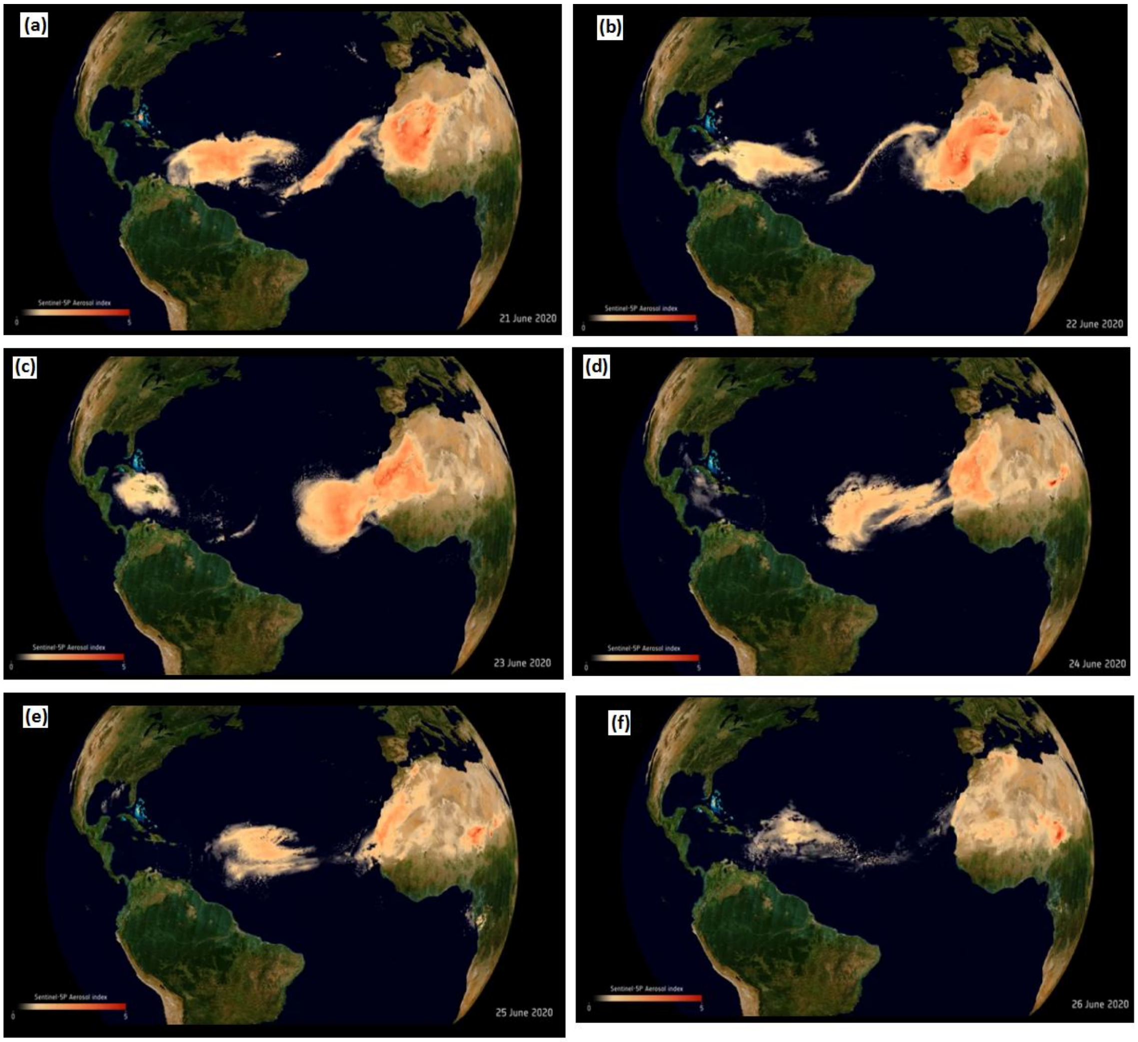

Figure 3:The Copernicus Sentinel-5P satellite images of Godzilla SDS over the Sahara for (a) 21.06.2020 (b) 22.06.2020 (c) 23.06.2020 (d) 24.06.2020 (e) 25.06.2020 (f) 26.06.2020 (European space Agency, 2020)

3.2. The variation of solar wind parameters between 15th and 26th June 2020

Figure 4 depicts the changes in IMF Bz, IEF Ey, the solar wind speed, K_p and Dst indices between 15th and 26th June 2020.

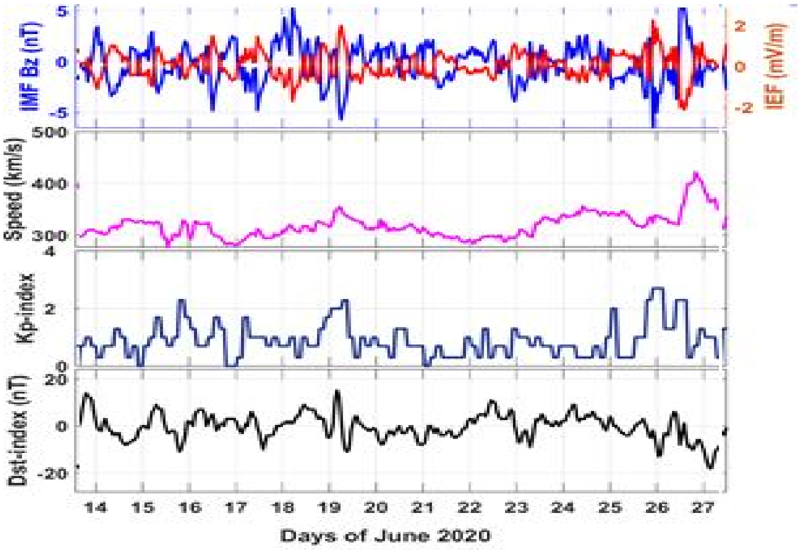

Figure4: Variations of Solar wind parameters; IMF-Bz, IEF-Ey and the solar wind speed and the geomagnetic indices; K_p and Dst index, between 15th and 26th June 2020

It is noted from Figure 4that, on 15th June 2020, there was a southward turning of the IMF-Bz of -3 nT with a corresponding rise of IEF-Ey of 1. The solar wind speed rose to maximum, of 330 km/s. The highest kp index value of 1.5 and lowest Dst value of -8 nT were attained. On 16th June 2020, the southward turning of -2.5 nT was attained with a corresponding rise in IEF-Ey of 1.5. The lowest solar wind speed of 280 km/s was attained. The maximum Kp index value attained was 2.2 with minimum Dst value of -11 nT. On 17th and 18th June 2020 there was a southward turning of -5 nT with a corresponding IEF-Ey of 1. The solar wind speed dropped from 320 km/s to 280 km/s on 17th June and rose to a maximum of 320 km/s on 18th June 2020. The maximum Dst value of 1.8 nT were attained on 17th and 18th June with a corresponding Dst value of -10 nT. On 20th June 2020, the IMF-Bz southern turning reached -6 nT with a corresponding IEF-Ey value of 2. This corresponded well with a solar wind speed of 350km/s. Between 15th and 26th June 2020, the highest Kp value of 2.2 was attained with a corresponding Dst index value of -11 nT on 19th June 2020. The The solar wind parameter shows a minimum solar wind speed of 270 km/s on 16th June 2020 and maximum solar wind of 360 km/s on 20th June 2020. During solar minimum, solar wind of speeds between 250 km/s and 400 km/s originates from regions close to the heliospheric current sheet at the heliomagnetic equator while the fast solar wind having speeds of between 400 km/s and 800 km/s which originates from coronal holes when the magnetic field is open[41]. The solar wind parameters and geomagnetic indices in Figure 4indicate a very minimalgeomagnetic field influence on the ionosphere between 15th and 26th June 2020.

3.3. Variations of TEC and $VTEC_{fit}$against UT

Figures 5and 6 shows the VTEC and $VTEC_{fit}$ against UT for OUCA-IFR1-TETN receiverarray while Figures 7 and 8 shows the VTEC and $VTEC_{fit}$ against UT for IFR1-MELI-TETN receiver array between 15th and 26th June 2020respectively.

3.3.1 OUCA-IFR1-TETN receiver array

From the OUCA-IFR1-TETN receiver array in Figures 5 and 6, it should be noted thaton 15th, 23rd and 24thJune 2020 triple peak structures(indicated by black arrows) wereobserved between 7:00 and 21:00 UT with the first peaks appearing between 7:00 and 9:00 UT, the second peaks appearing between 15:00 and 17:00 UT while the third peaks appearing between 19:00 and 21:00 UT. From 16th to 20th June 2020, double peak structures were observedbetween 07:00 and 12:00 UT with the first peaks appearing between 7:00 and 9:00 UT and the second peaks appearing between 18:00 and 21:00 UT.On 16th, 17th, 18th, 19th , 21st , 22nd, 25th and 26th June 2020, double peak structures however were observed between 7:00 and 12:00 UT with the first peaks appearing between 7:00 and 9:00 UT and the second peak appearing between 18:00 and 21:00 UT.

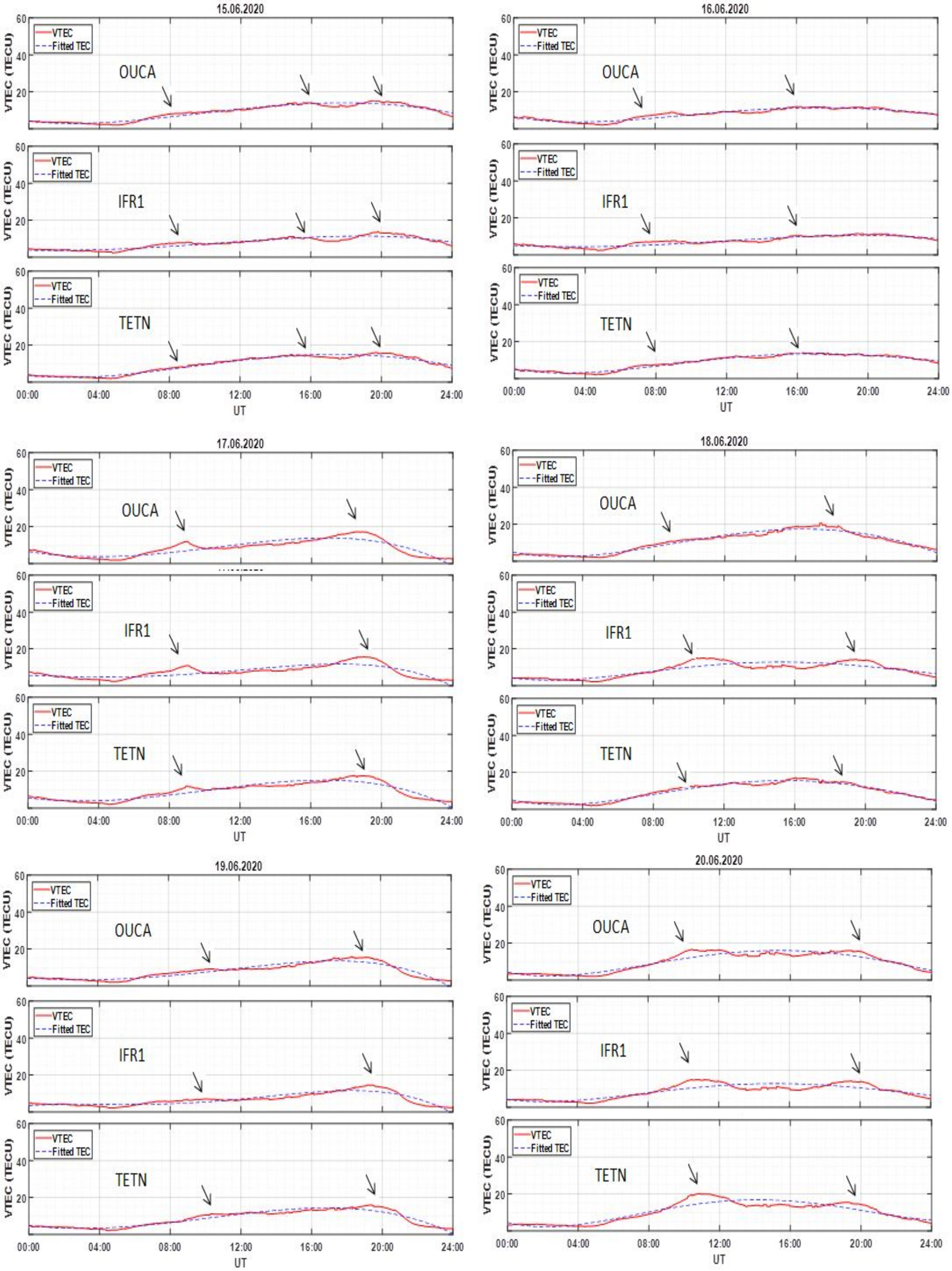

Figure5: VTEC and $VTEC_{fit}$ against UT for OUCA-IFR1-TETN receiver array between 15^{th} and 20^{th} June 2020

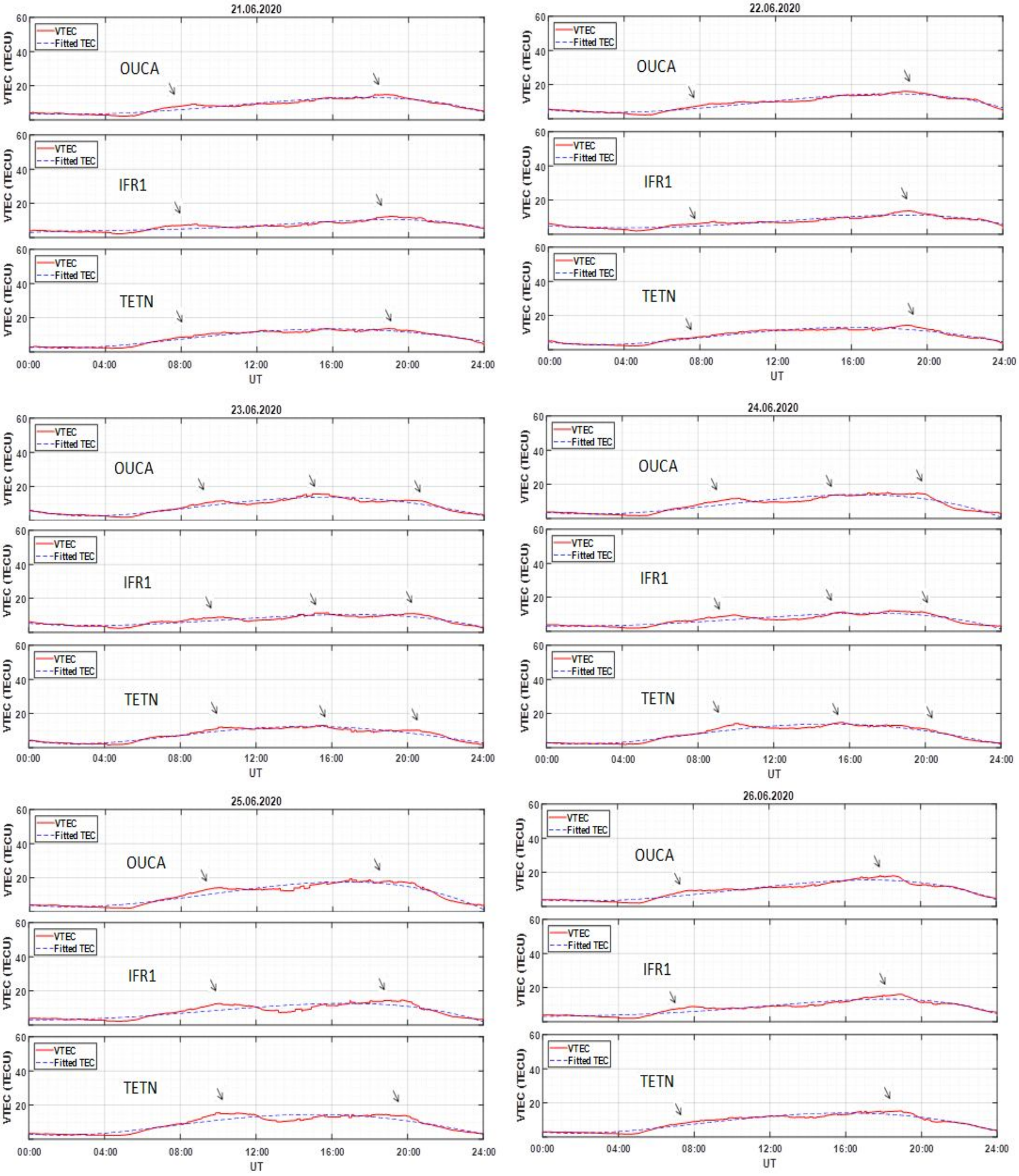

Figure 6: VTEC and VTEC$_{fit}$ against UT for OUCA-IFR1-TETN receiver array between 21st and 26th June 2020

3.3.2 IFR1-MELI-TETN receiver array

For the IFR1- MELI-TETN receiver arrays in Figures 7 and 8, it was also noted that on 15th , 23rd and 24th June 2020, triple peak structures were observed between 7:00 and 21:00 UT with the first peaks appearing between 7:00 and 9:00 UT, the second peaks appearing between 15:00 and 17:00 UT while the third peaks appearing between 19:00 and 21:00 UT Double peaks were observed on 16th, 17th, 18th, 19th, 20th, 21st, 22nd, 25th and 26th June 2020 with the first peak appearing between 08:00 and 12:00 UT while the thick peak appeared between 16:00 and 20:00 UT. A close analysis of Figure 5, 6, 7 and 8showed that the two receiver arrays exhibited similar wave-like structures. The peaks were observed to all appear between 7:00 and 12:00UT after sunrise and between 18:00 and 21:00UT after sunset.

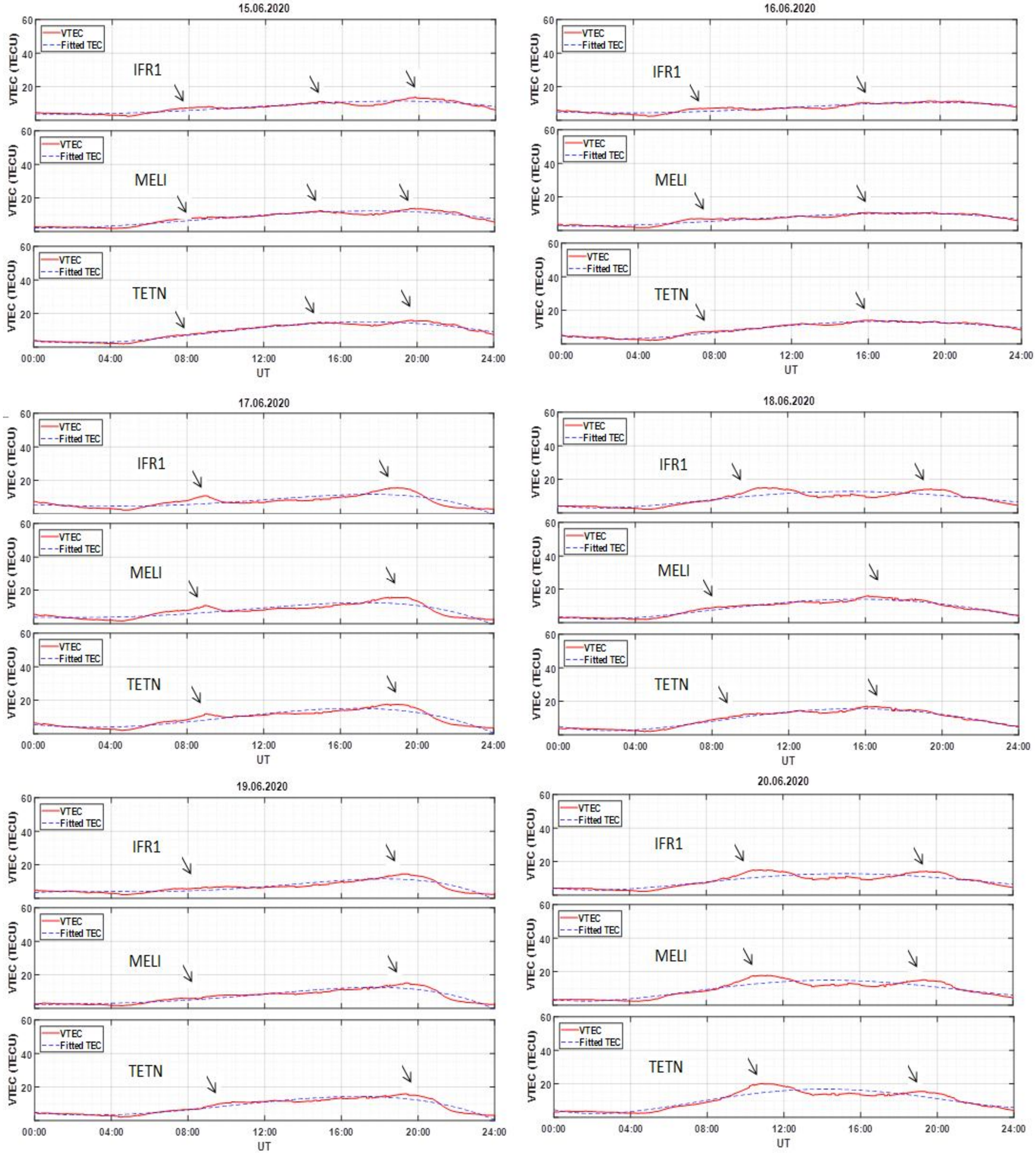

Figure7: VTEC and VTEC$_{fit}$ against UT for IFR1-MELI-TETN receiver array between 15th and 20th June 2020

It was also noted that the two receiver arrays shows peaks structures for the lower latitude stations (OUCA and IFR1) being observed first as compared to the other receiver stations. This indicates that there was a pole-ward propagation of the TIDs.

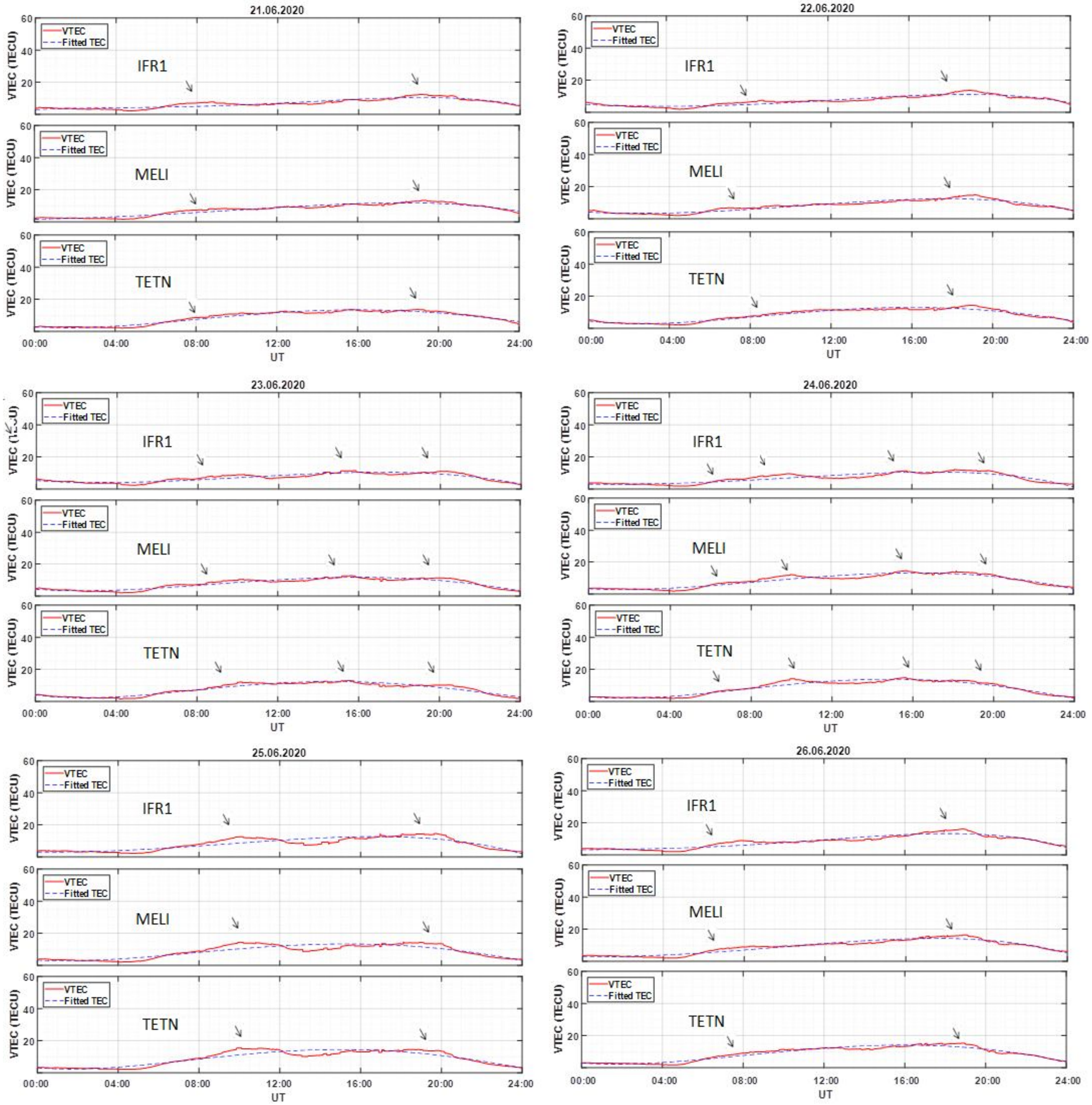

Figure 8: $VTEC$ and $VTEC_{fit}$ against UT for IFR1-MELI-TETN receiver array between 21st and 26th June 2020

3.4 Changes in detrended TEC (∆TEC)

Figures 9 to 14 show plots of detrended TECalong geographic latitude against UT for the four GNSS receiver stations between 15th and 26th June 2020.

In these Figures, band structures were observed over the 24 hour period for all the days between 15th and 26th June 2020. In Figure 9(a), 9(b), 11(b), 12(a) and 12(b) the band structures for DTEC ranged between 0.5 and 1.0 TECU. In Figure 10(a), 10(b), 11(a), 13(a), 13(b) the band structures for DTEC ranged between 0.6 and 1.5 TECU. In Figures 14(a) and 14(b), the band structures for DTEC ranged between 0.5 and 1.2 TECU.

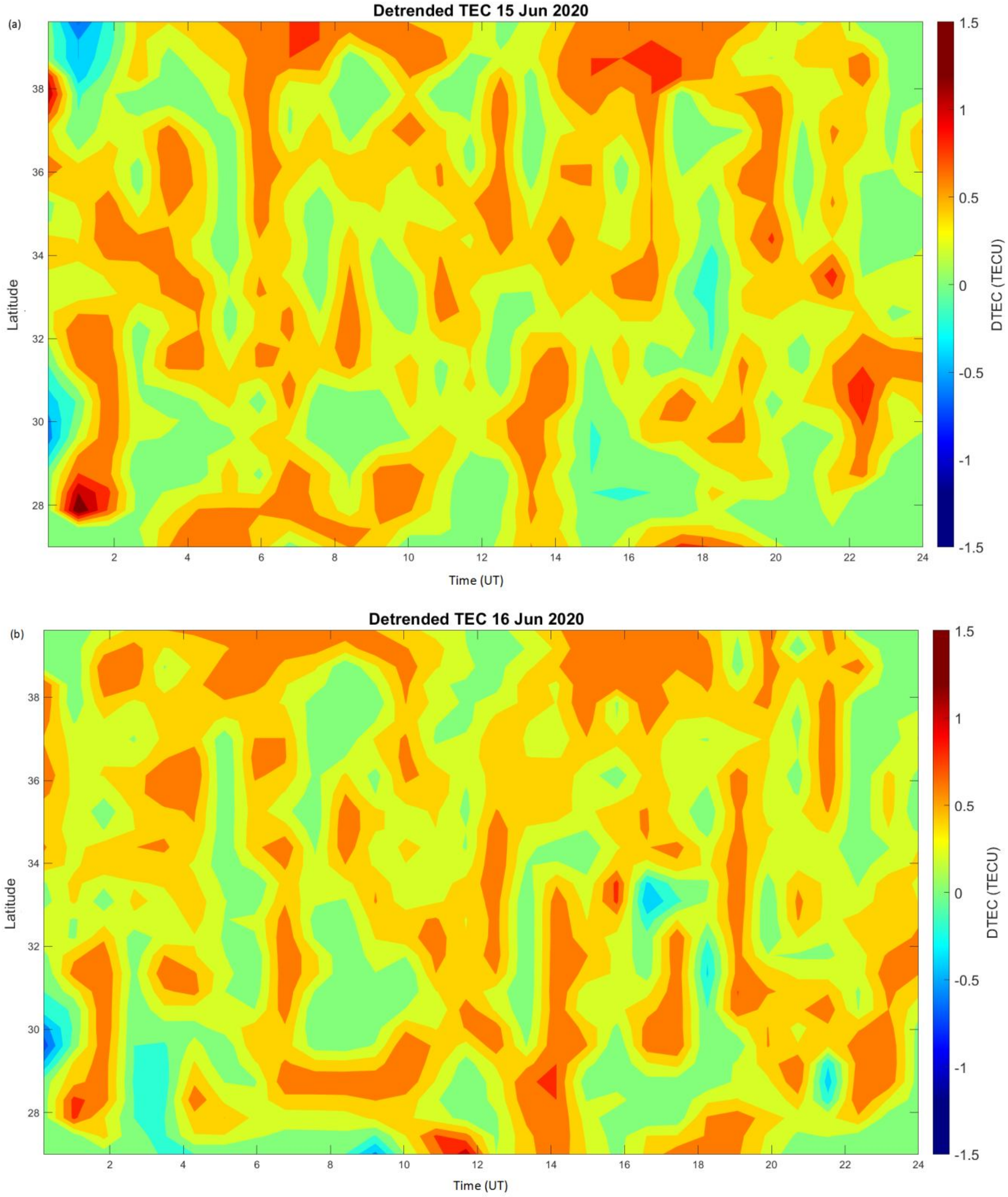

Figure 9: Plot of detrended TEC alonggeographic latitudes against UT for: (a) 15.06.2020, (b) 16.06.2020

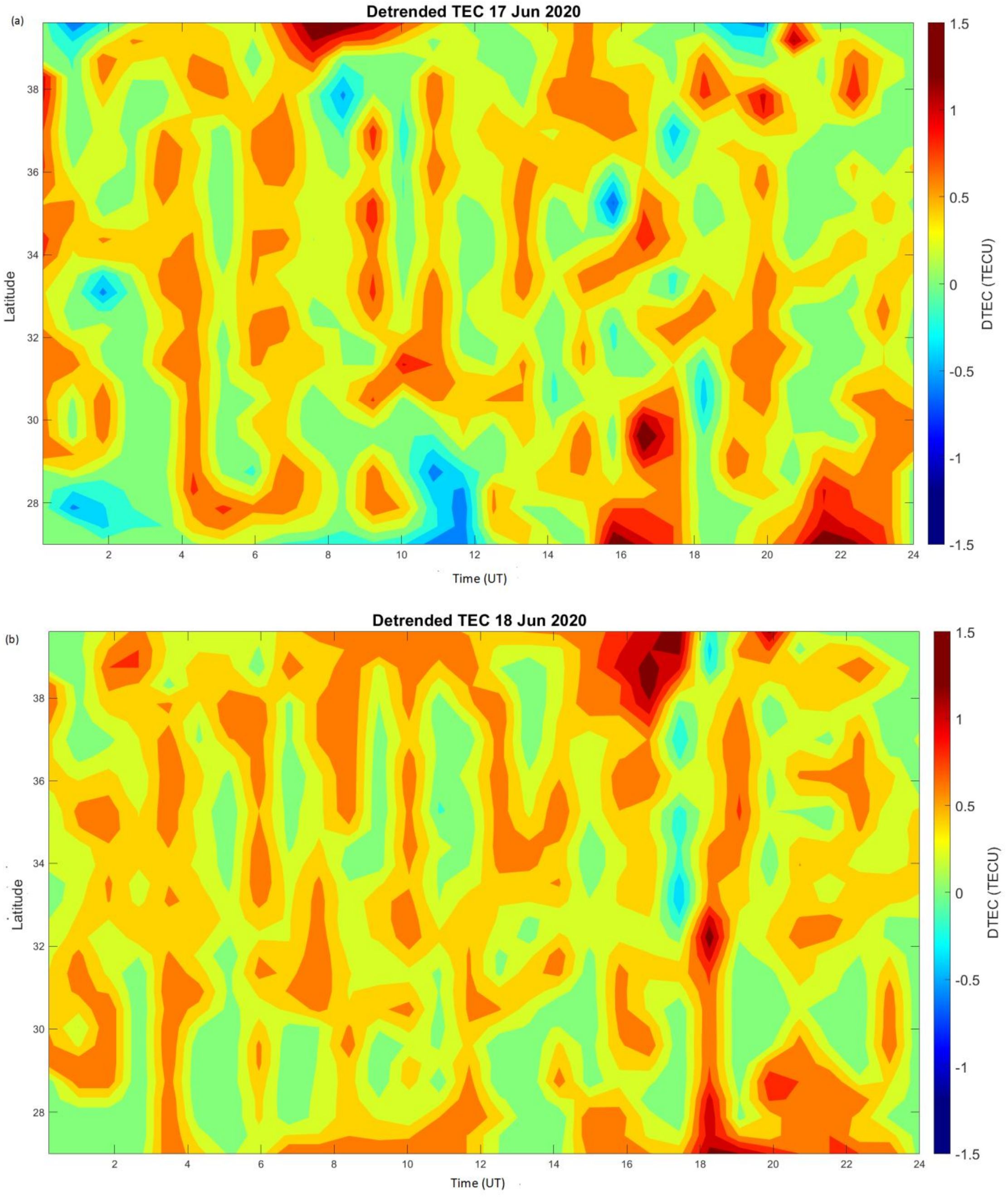

Figure 10: Plot of detrended TEC along geographic latitudes against UT for:(a) 17.06.2020 (b) 18.06.2020

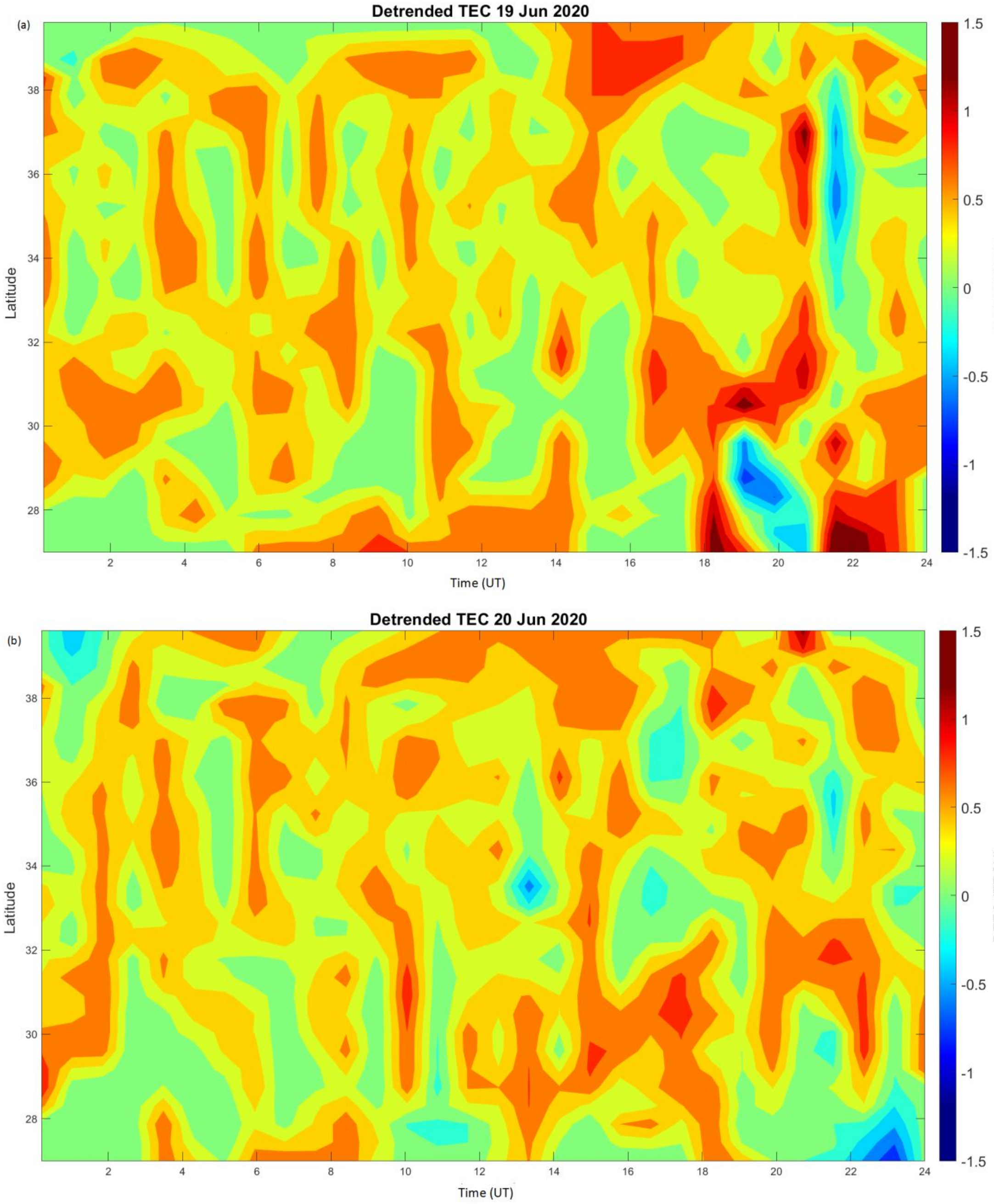

Figure 11: Plot of detrended TEC alonggeographic latitudes against UT for: (a) 19.06.2020 (b) 20.06.2020

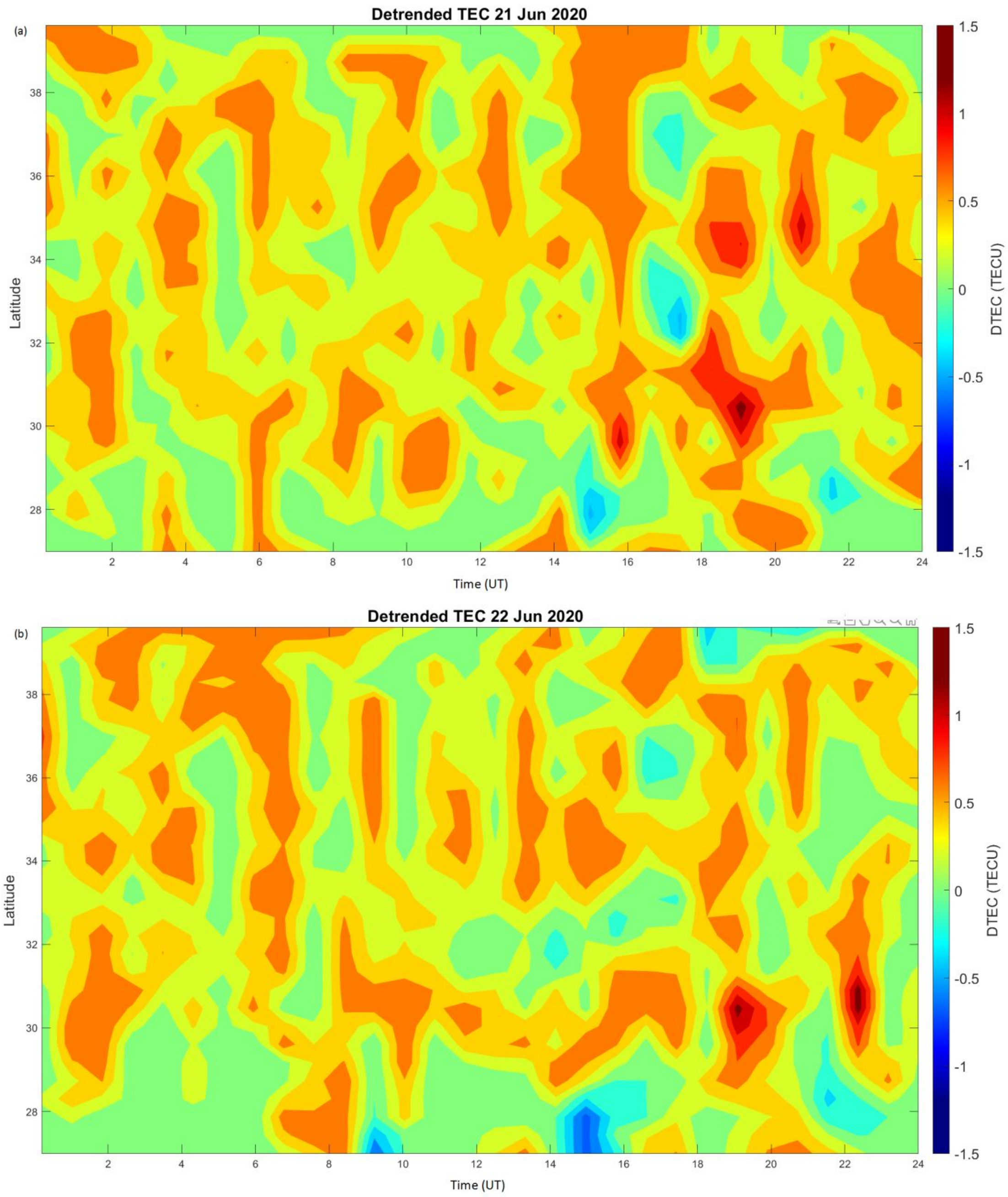

Figure 12: Plot of detrended TEC along geographic latitudes against UT for: (a) 21.06.2020 (b) 22.06.2020

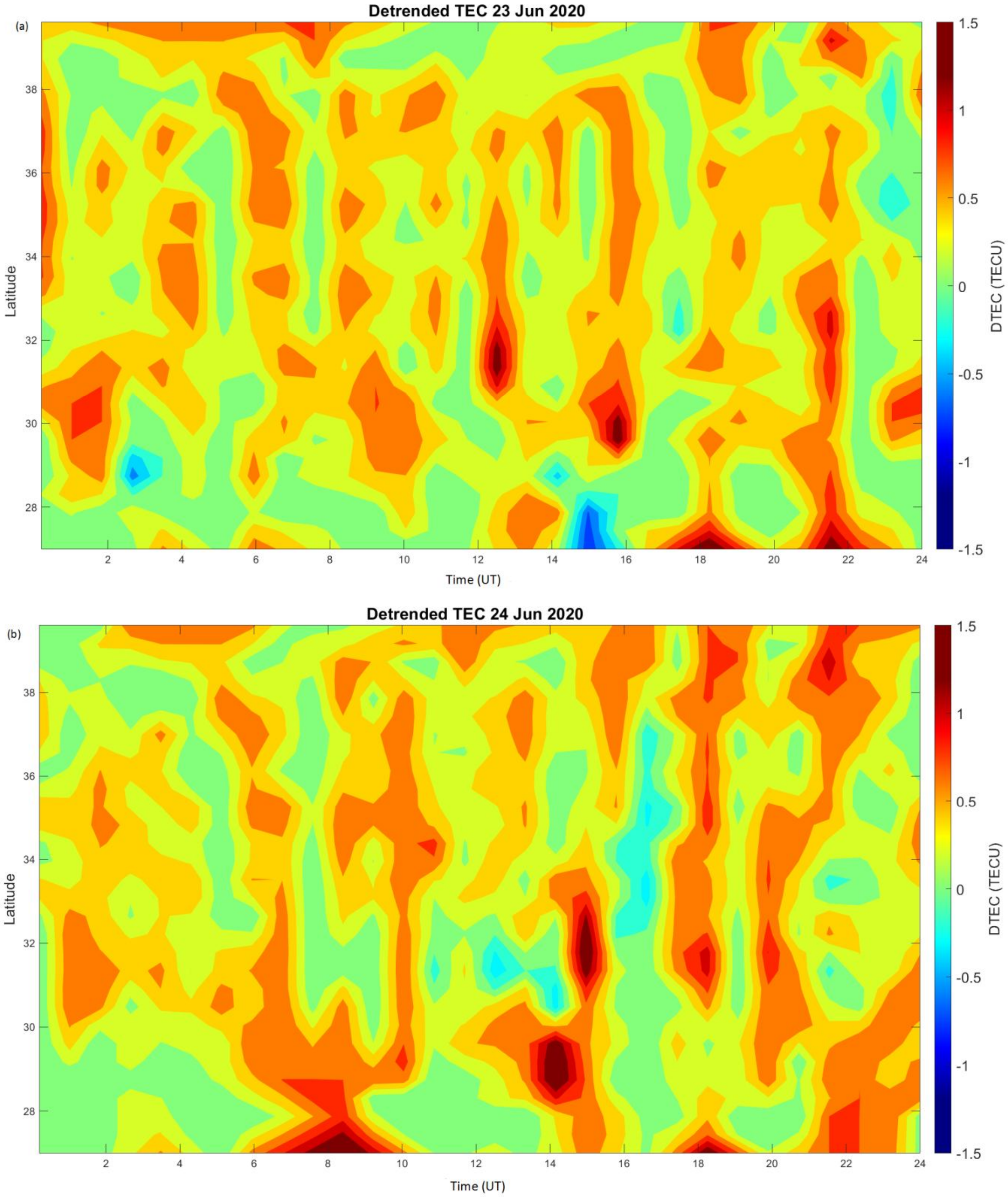

Figure 13: Plot of detrended TEC alonggeographic latitudes against UT for: (a) 23.06.2020 (b) 24.06.2020

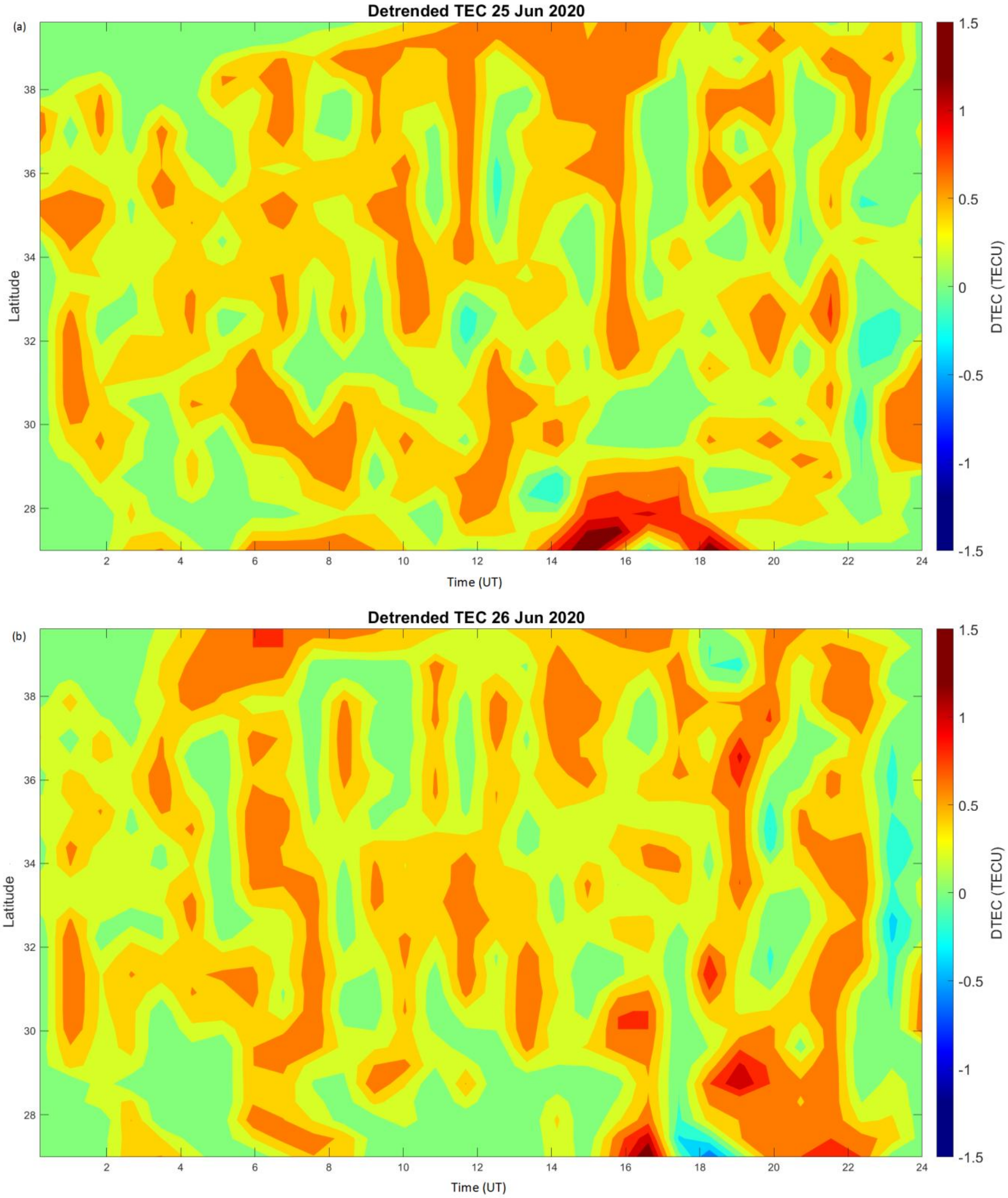

Figure 14: Plot of detrended TEC alonggeographic latitudes against UT for: (a) 25.06.2020 (b) 26.06.2020

In Figures 9, 10, 11, 12, 13 and 14, we can observe evident poleward propagating band structures during the 24 hour period for all the days between 15th and 26th June 2020. The band structures depicts present of TIDs.We also observe important values of detrended DTEC at the time of VTEC peaks. For example, Figures 10(a) and 11(a) show DTEC values of above 1 when VTEC has the large peaks around 18:00 UT. The band structures depict presence of TIDs that is important when VTEC is maximum.

The present study successfully demonstrates that SDS events are a source of energetics for generation of TIDs which are signatures of AGWs. The Dst and Kp indices in Figure 4 rules out the influence of geomagnetic activity in the generation of TIDs. Therefore the TEC results from this study exclude the effect of geomagnetic disturbances but are fully attributrd to the effect of the SDS.During SDS events, internal waves are continuously generated andbreaking throughout the atmosphere[11]. Wave breaking effectively mixes sand and dust aerosols through the atmosphere and contributes todriving some larger-scale flows. The gravity waves (GWs) generated are affected by the changing stratification as they propagate. Each of these interactions, inaddition to gravity wave dissipation, may contribute tothe vertical flux of horizontal momentum and the universal frequency spectrum inthe middle atmosphere [42,43,44, 45].The possible cause of these types of disturbances is the neutral winds [46]. Neutral winds plays an important role in the wave breaking/dissipation in the mesosphere and lower thermosphere to global redistribution of energy and momentum deposited at high latitudes by the magnetosphere[47]. They are usually slower than the actual wind in stable conditions and faster in unstable conditions i.e. land surface or sea stress.When GWs propagate into the ionosphere, the measured TEC exhibit clear wavelike structures, as shown in Figures 5, 6, 7 and 8. Their peaks and troughs areimaged on the ionospheric pierce points (IPP) trajectory at different moments and different propagation distances. Thismakes observation of GWs propagation possible.

3. CONCLUSION

We have investigated the generation of TIDs during the Godzilla SDS event of June 2020 over Morocco using GPS-TEC data. The obtained results showed TEC exhibited wave-like structures having distinct troughs and peaks over IFR1-MELI-TETN and OUCA-IFR1-TETN arrays which were clear indicators of generation of TIDs. The arrays showed that the TIDs propagated poleward (along latitude). This was supported by the evident poleward propagating band structures on the detrended TEC plots during the 24 hour period for all the days between 15th and 26th June 2020. The band structures on the plots also depictedthe presence of TIDs.Neutral winds were seen to play a very important role in the propagation of the AGWs which are manifestations of TIDs. In conclusion, the study confirms that SDS events can be a source of energetics for the generation of MSTIDs.

REFERENCES

[1] Hines, C. O. (1960). Internal atmospheric gravity waves at ionosphericheights, Can. J Phys., 38, 1414.

[2] Hines, C. O. (1974). The upper atmosphere in motion, GeophysicalMonograph, American Geophysical Union.

[3] Hocke, K., and K. Schlegel. (1996). A review of atmospheric gravity wavesand travelling ionospheric disturbances: 1982–1995, AnnalesGeophysicae, 14, 917.

[4] Tsagouri, I., Belehaki, A., Koutroumbas, K., Herekakis, T. (2023). Identification of Large Scale Ionospheric Travelling Disturbances (LSTIDs) based on Digisonde observations. Atmosphere 2023, 14, 331.https://doi.org/10.3390/atmos14020331.

[5] Richmond, A. D.(1978). Gravity wave generation, propagation, anddissipation in the thermosphere, J. Geophys. Res., 83, 4131.

[6]Hunsucker, R. D.(1982)Atmospheric gravity waves generated in thehigh latitude ionosphere: a review, Rev. Geophys. Space Phys.,20, 293.

[7] Jing,N.,and R.D.Hunsucker(1993). A theoretical investigation ofsources of large and medium scale atmospheric gravity waves in the auroral oval, J.Atmos. Terr. Phys., 55, 1667.

[8] Balthazor, R. L., Moffett R. J. (1997). A study of atmospheric gravity waves and travelling ionospheric disturbances at equatorial latitudes. Annales Geophysicae, 15, 1048-1056.

[9] Ding, F., Wan, W., Ning, B., Zhao, B., Li, Q., Zhang, R., Xiong, B. and Song, B.(2012). Two dimensional imaging of large scale travelling ionospheric disturbances over China based on GPS data. J. Geophys. Res. 2012, 117, A08318.

[10] Ferreira, A. A., Borries, C., Xiong, C., Borges, R. A., Mielich, J. and Kouba, D. (2022). Identification of potential precursors for the occurrence of large scale travelling Ionospheric disturbances in a case study during September 2017. J. Space weather . Space Clim. 2020, 10, 32.

[11]Fritts, D. C. & Yuan, L. (1989). Stability analysis of inertia-wave structure in the middle atmosphere. Journal of atmospheric sciences, 46(12), 1738-1745. https://doi.org/10.1175/1520-0469(1989)046<1738:saoiws>2.0.co;2.

[15] Katamzi, Z. T. & Habarulema, J. B. (2014). Travelling Ionospheric Disturbances observed At South African mid-latitudes during the 29th – 31st October 2003 geomagnetically Disturbed period. Advances in space Research 53, (2014) 48-62.

[12] Kotake, N., Otsuka, Y., Tsugawa, T., Ogawa, T. and Saito, A. (2006). Climatological study of GPS total electron content variations caused by medium-scale travelling ionospheric disturbances. J. Geophys. Res. 2006, 111, 1-8.

[13] Frissell, N. A., Baker, J. B. H., Ruohoniemi, J. M., Greenwald, R. A., Gerrard, A. J., Miller, E. S and West, M. L. (2016). Sources and characteristics of medium-scale travelling ionospheric disturbances observed by high frequency radars in the North America Sector. J. Geophys. Res. Space Physics 2016, 121, 3722-3739.

[14] Habarulema, J. B., Katamzi, Z. T., Yingezaw, E., Yamazaki, Y., Seemala, G. (2016). Simultaneous storm time equatorward and poleward large scale TIDs on a global scale. Geophysical Research letters, Vol. 43, no. 13, pp.6678-6686.

[15] Habarulema, J. B., McKinnell, L-A., Buresova, D., Zhang, Y., Seemala, G., Ngwira, C., Chum, J., Opperman, B. (2013). A comparative study of TEC response for the African equatorial and mid-latitudes during storm conditions. Journal of Atmospheric Solar-Terrestrial physics, 102:105-114.

[16] McNamara, L. (1991). The ionosphere: Communications, Surveillance and direction findingOrbit, a foundation series. Krieger Pub. Co.

[17] Gorelick, N., Hancher, M.,Dixon, M., Ilyushchenko, S., Thau, D., Moore, R. (2017). Google Earth Engine: Planetary-scale geospatial analysis for everyone. Remote sensing and Environment, 202, 18-27.

[18] De Graaf, M., Stammes, P., Torres, O., Koelemeijer, R. B. A. (2005). Absorbing Aerosol Index: Sensitivity analysis, application to GOME, and comparison to TOMS. Journal of Geophysical Research: Atmospheres, 110(D1).

[19] Zhongming, Z., Linong, L., Xiaona, Y., Wangqiang, Z., Wei, L. (2020). Satellites and Unusual Sahara dust plume.

[20] Asare-Ansah, A. B., Twumasi, Y. A., Ning, Z. H., Ansah, P. B., Frimpong, D. B., Owusu, F., Apraku, C. Y., Anokye, M., Loh, M., Armah, R. D. N., Opong, J. (2022). Tracking The Godzilla Dust plume using the Google Earth Engine Platform. The international Archives of the photogrammetry, Remote sensing and spatial information sciences, Vol. XLVI-M-2-2022, ASPRS 2022 Annual conference, 6-8 February and 21-25 March 2022, Denver, Colorado, USA and Virtual. https://doi.org/10.5194/isprs-Archives-XLVI-M-2-2022-33-2022.

[21] Althaf, P., Shaeb, K. H. B., Kumar, K. R. (2022). Hotspot analysis and long-term trends of Absorbing aerosol index from dust emissions were measured by the Ozone measuring Instrument at different Urban locations in India from 2005 to 2008. Atmospheric environment. 118933.

[22] Jethva, H.,Satheesh, S. K., Srinivasan, J. (2005). Seasonal variability of aerosols over the Indo-Gangetic basin. Journal of Geophysical Research: Atmospheres, 110(D21).

[23] Gorelick, N., Hancher, M.,Dixon, M., Ilyushchenko, S., Thau, D., Moore, R. (2017). Google Earth Engine: Planetary-scale geospatial analysis for everyone. Remote sensing and Environment, 202, 18-27.

[24] Gurtner, W., Estey, L. (2007) Rinex-the receiver independent exchange format-version 3.00. Astronomical Institute, University of Bern and UNAVCO, Bolulder, Colorado.

[25] Seemala, G. K. (2011). GPS-TEC Analysis Application Read Me. Institute for Scientific Research, Boston college, USA.

[26] Tariku YA (2015) Patterns of gps-tec variation over low-latitude regions (African sector) during the deep solar minimum (2008 to 2009) and solar maximum (2012 to 2013) phases. Earth, Planets and Space 67(1):1–9.

[27] Horvath I, Crozier S (2007) Software developed for obtaining GPS-derived total electron content values. Radio Science 42(02):1–20

[28] Cepni, M. S., Potts, L. V., Miima, J. B. (2013) High-resolution station-based diurnal ionospheric total electron content (TEC) from dual-frequency GPS observation Space Weather 11(9):520–528.

[29] Ma X, Maruyama T, Ma G, et al (2005) Three-dimensional ionospheric tomography using observation data of gps ground receivers and ionosonde by neural network. Journal of Geophysical Research: Space Physics 110(A5).

[30] Jin, S., Park, J., Wang, J., Choi, B. and Park, P. (2006). Electron density profiles derived from ground-based observations. The Journal of Navigation 59(3): 395-401.

[31] Heise S, Jakowski N, Wehrenpfennig A, et al (2002) Sounding of the topside ionosphere/ plasmasphere based on GPS measurements from champ: Initial results. Geophysical Research Letters 29(14):44–1.

[32] Jawoski, N., Mayer, C., Hoque, M. and Wilken, V. (2011). Total electron content models Andtheir use in ionosphere monitoring. Radio science, 46(06): 1-11.

[33] Ciraolo, L., Azpilicueta, F., Brunini, C., Meza, A. and Radicella, S. M. (2007). Calibration errors on experimental slant total electron content determined by the GPS. Journal of Geodesy, 81:111-120.

[34] Kassa, T., Damtie, B., Ionospheric irregularities over Bahir Dar, Ethiopia during selected geomagnetic storms, Advances in Space Research (2017), doi: http://dx.doi.org/10.1016/j.asr.2017.03.036.

[35] Otsuka, Y., Ogawa, T., Saito, A., Tsugawa, T., Fukao, S., Miyazaki, S. (2002). A new technique for mapping of total electron content using GPS network in Japan. Earth, Planets and space. 54(1): 63-70.

[36] Sardon, E. and Zarraoa, N. (1997). Estimation of total electron using GPS data: How stable are the differential satellite and receiver instrumental biases? Radioscience, vol. 32, No.5, pp. 1899-1910.

[37] Aryal, S., Geddes, G., Finn, S., et al., (2019). Multi-spectral and Multi-instrumentation Observation of TIDs following the solar eclipse of 21st August 2017.Journal of Geophysical Research: Space Physics, vol. 124.

[38] Zhang, S. R., Coaster, A. J., Erickson, P. J., Goncharenko, L. P., Rideout, W. & Vierinen, J. (2019). Travelling ionospheric disturbances and ionospheric perturbations associated with solar flares in September 2017. Journal of Geographical Research: Space physics, 124(7), 5894-5917.

[39] Zakharenkova, I., Astafyeava, E. & Cherniak, I. (2016). GPS and GLONAS observations of lareg-scale travelling ionopspheric disturbances during the 2015 St. Patrick’s day storm. Journal of Geophysical Research: Space physics, 121(12), 12-138. https://doi.org/10.1002/2016ja032332.

[40] Warren, C. (2022). Godzilla dust storm traced to shaky northern jet stream. Retrieved May 2023, from science: https://www.science.org/content/article/godzilla-dust-storm-Traced-shaky-northern-jet-stream.

[41] Kamide, Y. and Chian, A.(2007).Hand Book of the Solar-Terrestrial environment. SpringerBerlin Heidelberg, New York.ISBN 978-3-540-46314-6.Doi:10.007/6104478.

[42] VanZandt, T. E., 1982: A universal spectrum of buoyancy waves in the atmosphere. *Geophys. Res. Lett.*, **9**, 575-578.

[43] Balsley, B. B., and Carter, D. A., 1982: The spectrum of atmospheric velocity fluctuations at 8 and 86 km. *Geophys. Res. Lett.*, **9**, 465–468.

[44] Nakamura, T., Tsuda, T., Fukao, S., Kato, S., Manson, A. H., and Meek, C. E., 1993: Comparative observations of short-period gravity waves (10-100 min) in the mesosphere in 1989 by Saskatoon MF radar (52*o*n), Canada and the MU radar (35*o*n), Japan. *Radio Sci.*, **28**, 729–746.

[45] Collins, R. L., Nomura, A., and Gardner, C. S., 1994: Gravity waves in the upper mesosphere over Antarctica: Lidar observations at the South Pole and Syowa. *J. Geophys. Res.*, **99**, 5475–5485.

[46] Jonah, O.F.; Zhang, S.; Coster, A.J.; Goncharenko, L.P.; Erickson, P.J.; Rideout, W.; de Paula, E.R.; de Jesus, R. (2020). Understanding Inter-Hemispheric Traveling Ionospheric Disturbances and Their Mechanisms. *Remote Sens.*, *12*, 228.

[47] Dhadly M, Sassi F, Emmert J, Drob D, Conde M, Wu Q, Makela J, Budzien S and Nicholas A (2023), Neutral winds frommesosphere to thermosphere—past, present, and future outlook. *Front. Astron. Space Sci.* 9:1050586. doi: 10.3389/fspas.2022.1050586.